

Parachute Dynamic Stability and the Effects of Apparent Inertia

Jason M. Ginn*

Georgia Institute of Technology, Atlanta, GA, 30332

Ian G. Clark†

Jet Propulsion Laboratory, California Institute of Technology, Pasadena, CA, 91109

Robert D. Braun ‡

Georgia Institute of Technology, Atlanta, GA, 30332

The dynamic stability and equilibrium conditions of a parachute are studied using a six degree of freedom dynamic model that includes apparent inertia effects. Existing parachute dynamic models are discussed and the selection of a relevant model is shown. The chosen dynamic model that incorporates apparent inertia is summarized and used for analysis. The moments on the parachute system caused by the apparent inertia term are shown to affect both the equilibrium point and the stability of the system. The adjustment to equilibrium is observed and discussed. A small disturbance stability analysis is performed to give a stability criterion in terms of the slope of the tangential aerodynamic force. The dynamic modes, pitching and coning, are discussed. Computational integration of the equations of motion is used to validate the small disturbance analysis as well as to show the effects of large disturbances.

Nomenclature

A_{ij}	Component of apparent inertia tensor
C_N	Normal force coefficient
C_{N_α}	Slope of the normal force coefficient at $\alpha = \alpha_0$
C_T	Tangential force coefficient
C_{T_0}	Tangential force coefficient at $\alpha = 0$
C_{T_α}	Slope of the tangential force coefficient at $\alpha = \alpha_0$
D_P	Projected diameter of the canopy
g	Acceleration due to gravity
h_i	Angular momentum in the i^{th} direction
$I_{6 \times 6}$	Generalized 6x6 inertia tensor
I_{xx}	Second moment of inertia about x axis
K_1	First moment of inertia about x, y axes
K_{ij}	Nondimensionalized apparent inertia tensor value
k	Apparent inertia scaling factor
m	Mass of the system
O	Origin of body-fixed coordinate system
p, q, r	Rotation about the body-fixed x, y, z axes
p_i	Linear momentum in the i^{th} direction
u_i^o	Generalized velocity component of O with respect to an inertial frame

*Graduate Student, Guggenheim School of Aerospace Engineering, AIAA Student Member.

†LDS Principal Investigator, AIAA Member.

‡David and Andrew Lewis Professor of Space Technology, Guggenheim School of Aerospace Engineering, AIAA Fellow.

T_F	Kinetic energy of the fluid
u, v, w	Velocity in the x, y, z directions with respect to the body-fixed coordinate frame
\vec{V}	Translational velocity of O with respect to an inertial frame
V	Magnitude of velocity
x, y, z	Position coordinates with respect to the body-fixed coordinate frame
z_{CG}	Distance from the origin of the body-fixed coordinate system to the center of mass
α	Angle of attack at the center of pressure of the canopy
α_0	Angle of attack where $C_N = 0$
ϕ, θ	Rotations about x, y using an x - y - z Euler angle convention
ρ	Density at the canopy

Subscripts

E	Equilibrium quantity
0	Baseline quantity

Superscripts

'	Disturbance variable
---	----------------------

I. Introduction

The Low Density Supersonic Decelerator (LSD) project has been tasked with the development of a new supersonic parachute for use on future Mars missions.¹ This new design must increase the amount of mass than can be delivered to the surface by increasing the total drag force. The stability of the parachute system must also be considered for a variety of reasons, such as system safety or the ability to accurately track the ground for a precise landing. Throughout the design process, the effects of the low density of the Martian atmosphere on stability have been considered. It was found that few studies have been done on how parachute dynamics are affected by apparent inertia.

Apparent inertia can be described as the added inertia that the parachute feels due to the mass of the air. As this effect scales with the density of the fluid, it provides relevant insight to the differences between low altitude Earth testing and Mars flight. Although some studies have incorporated the apparent inertia tensor into a parachute dynamics model,²⁻⁴ there has not been a stability analysis using these effects or a comparison of the stability characteristics to traditional parachute models that neglect these effects. The goal of this paper is to characterize the apparent inertia effects on parachute stability.

Previous analyses of parachute dynamics generally use models that range from 3 degrees of freedom (DoF) planar models to 9 DoF wrist mode models. A common dynamic model used for analytical studies is the 5 DoF White-Wolf⁵ model. This model includes apparent inertia terms but does not include the full tensor form and its effects. For full trajectory simulation, a 9 DoF model is frequently used that assumes two rigid bodies (the canopy and the payload) that can pivot about the bridle.⁶

A. Eaton Parachute Dynamics Model

The parachute dynamics model presented by Eaton² was selected to study. This 6 DoF model includes apparent inertia in its tensor form and has been shown to provide a good match to experimental flight data. The inclusion of apparent inertia is of importance as it affects the design of parachute systems to be used for entry, descent, and landing at other planets. This is of specific importance when designing parachutes for use at Mars, where the atmospheric density is much lower than that of Earth.

When a parachute and payload move through a fluid, the inertia of the air moving inside and around the canopy must be considered in addition to the system's own mass and moments of inertia. This inertia can be studied by defining apparent inertia as a 6x6 tensor with units of mass, first and second moments of inertia, and products of inertia. A rigid body inertia tensor is represented by a 6x6 symmetric matrix that describes the relationship between the body's momentum (both linear and angular) and its velocity components (also linear and angular), as shown in Eq. (1).⁷ Apparent inertia is defined similarly, however integration of the flowfield is required.

$$\begin{bmatrix} p_1 \\ p_2 \\ p_3 \\ h_1 \\ h_2 \\ h_3 \end{bmatrix} = I_{6 \times 6} \begin{bmatrix} u \\ v \\ w \\ p \\ q \\ r \end{bmatrix} \quad (1)$$

The tensor definition of apparent inertia is derived from potential flow theory using the kinetic energy of the fluid,² as shown in Eq. (2), which leads to the integral form of the apparent inertia tensor, Eq. (3). This definition requires integration throughout space and knowledge of the fluid density and velocity at every point. As this is difficult to do in practice, the tensor terms are commonly nondimensionalized in terms of the projected diameter and the fluid density at the canopy,² as shown in Eqs. (4)–(6). The resulting K_{ij} terms are then taken from experimental data and assumed to be constant for a given system. A few experiments have been performed to investigate the values of these constants,^{8,9} however many studies use empirical data. The K_{ij} values given in Table 1 were used for Eaton’s baseline simulation. These values were later changed by Eaton to $K_{11} = 0.3$ and $K_{33} = 0.6$ to provide a better match between simulation and flight data. The values for the K_{ij} coefficients appear to range between 0.2 and 1 in relevant studies.^{2,3,5} Additionally, the ratio $K_{33}/K_{11} = 2$ has been taken in multiple recent studies and appears to provide a good match with flight data.^{2,3}

$$T_F(t) = \sum_{i,j=1}^6 T_{F_{ij}}(\vec{V}, \rho) = \frac{1}{2} \sum_{i,j=1}^6 A_{ij}(\vec{V}, \rho) u_i^o(t) u_j^o(t) \quad (2)$$

$$A_{ij}(\vec{V}, \rho) = \frac{1}{u_i^o(t) u_j^o(t)} \int \int \int_R \rho(x, y, z, t) u_i(x, y, z, t) u_j(x, y, z, t) dR \quad (3)$$

$$K_{ii} = \frac{6A_{ii}}{\pi \rho D_p^3} \quad i = 1, 2, 3 \quad (4)$$

$$K_{ii} = \frac{60A_{ii}}{\pi \rho D_p^5} \quad i = 4, 5, 6 \quad (5)$$

$$K_{ij} = \frac{6A_{ij}}{\pi \rho D_p^4} \quad i \neq j \quad (6)$$

Eaton² provides the 6 DoF equations of motion that include the effects of the apparent inertia tensor and discusses the simplifications that can be made if various symmetry assumptions are made. For example, if the x-z plane is a plane of symmetry and the origin of the body-fixed axis lies in this plane, the A_{ij} interaction terms between the longitudinal variables (p_1, p_3, h_2, u, w, q) and the lateral terms (p_2, h_1, h_3, v, p, r) are zero, leaving 12 unique nonzero terms. Further simplifications can be made for the case of a parachute that is axisymmetric about the z axis, leaving only four unique nonzero terms. These terms are A_{11} ($= A_{22}$), A_{33} , A_{55} ($= A_{44}$), and A_{15} ($= A_{15} = -A_{24} = -A_{42}$).²

Eqs. (7) and (8) are the equations of motion for an axisymmetric parachute. This model assumes that the system is a rigid body. Additionally, the aerodynamic force on the payload will be neglected for this study. A body-fixed coordinate system is used with the z-direction pointing down the parachute and an origin at the center of pressure of the canopy, as shown in Figure 1. Due to the axisymmetric assumption, only four apparent inertia terms, (A_{11} , A_{33} , A_{55} , and A_{15}), are required. Eaton assumes that the A_{15} term is negligible, which has been assumed to be true for these studies as well. These equations introduce moments in the tangential directions due to differences in the apparent inertia terms. These moments appear even with the assumption of steady aerodynamics and represent a difference in the resistance to motion in different directions. If A_{33} is larger than A_{11} , the fluid inertia causes a moment that will turn the parachute such that the magnitude of w is reduced.

$$\sum \vec{F} = \begin{bmatrix} (m + A_{11})(\dot{u} - vr) + (m + A_{33})wq + (K_1 + A_{15})(\dot{q} + rp) \\ (m + A_{11})(\dot{v} - ur) - (m + A_{33})wp - (K_1 + A_{15})(\dot{p} - qr) \\ (m + A_{33})\dot{w} - (m + A_{11})(uq - vp) - (K_1 + A_{15})(p^2 + q^2) \end{bmatrix} \quad (7)$$

$$\sum \vec{M} = \begin{bmatrix} (I_{xx} + A_{55})\dot{p} - (K_1 + A_{15})(\dot{v} - wp - ur) - (I_{yy} + A_{55} - I_{zz})qr + (A_{33} - A_{11})vw \\ (I_{yy} + A_{55})\dot{q} + (K_1 + A_{15})(\dot{u} + wq - vr) + (I_{xx} + A_{55} - I_{zz})pr - (A_{33} - A_{11})uw \\ I_{zz}\dot{r} + (I_{yy} - I_{xx})pq \end{bmatrix} \quad (8)$$

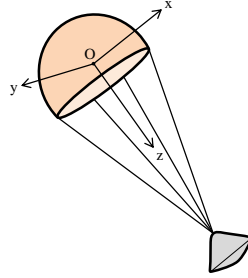


Figure 1. Diagram of the body-fixed coordinate frame.

II. Effects on Equilibrium Point

The apparent inertia moments unique to the Eaton model cause a noticeable effect on the equilibrium point of the system. For this discussion, the aerodynamic model given in Eq. (9) and Eq. (10) has been used. This was the model used by White and Wolf⁵ for their analysis of parachute stability. The selection of this model allows for a more direct comparison of the stability implied by the Eaton and White-Wolf models. These aerodynamic curves are shown in Figure 2 using the baseline parameters from Table 1. Note that α_0 is the angle of attack where the system is at aerodynamic trim.

$$C_N = C_{N_\alpha} \alpha \left(\frac{\alpha}{\alpha_0} - 1 \right) \quad (9)$$

$$C_T = C_{T_0} + \frac{1}{2} C_{T_\alpha} \alpha_0 \left(\frac{\alpha^2}{\alpha_0^2} - 1 \right) \quad (10)$$

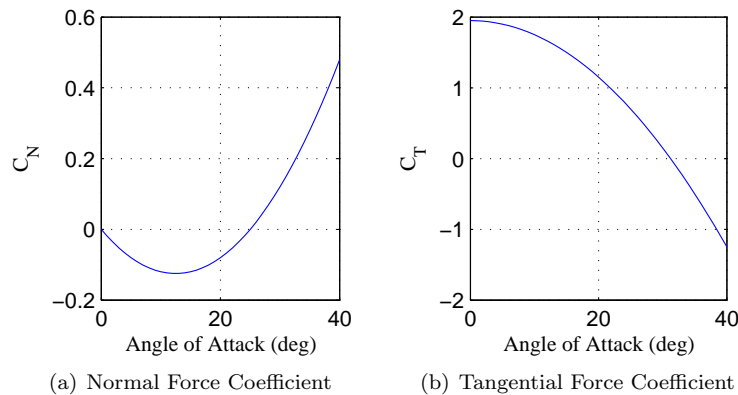


Figure 2. Assumed form of aerodynamic curves using values specified by Table 1.

For a traditional parachute dynamic model that does not incorporate the apparent inertia tensor and the resulting moment, the equilibrium state has two closed form solutions. The parachute can either be in a glide or in vertical descent with an angle of attack of zero. Typically, direct vertical descent is unstable due to the aerodynamics, so it will be considered a trivial solution. Eqs. (11), (12), and (13) provide the solution for

the gliding equilibrium state when the apparent inertia couple is neglected. The equilibrium velocity given is often referred to as the terminal velocity. Without the presence of the apparent inertia moments, the Euler angle θ is zero and the parachute will glide at an the trim angle of attack while in a vertical orientation.

$$\theta = 0 \quad (11)$$

$$\alpha = \alpha_0 \quad (12)$$

$$V = \sqrt{\frac{2mg}{\rho\pi\frac{D_P^2}{4}C_{T_0}}} \quad (13)$$

The Eaton dynamic model can be analyzed using a similar method. For the system to be in equilibrium, the derivatives of all state variables (excluding position), must be zero. For planar static stability, only θ , the velocity components u and w , and the position variables are allowed to be nonzero. When the zero values are inserted to the Eaton equations of motion, Eqs. (7) and (8), and the gravitational and aerodynamic forces and moments are applied, the equations for the equilibrium state can be found. These equations are shown in Eqs. (14)–(17).

$$\left[C_{N_\alpha} \alpha \left(\frac{\alpha}{\alpha_0} - 1 \right) \right] \frac{1}{2} \rho (u^2 + w^2) \pi \frac{D_P^2}{4} + mg \sin \theta = 0 \quad (14)$$

$$- \left[C_{T_0} + \frac{1}{2} C_{T_\alpha} \alpha_0 \left(\frac{\alpha^2}{\alpha_0^2} - 1 \right) \right] \frac{1}{2} \rho (u^2 + w^2) \pi \frac{D_P^2}{4} + mg \cos \theta = 0 \quad (15)$$

$$-z_{CG} mg \sin \theta + (A_{33} - A_{11}) uw = 0 \quad (16)$$

$$\alpha = \tan^{-1} \left(\frac{u}{w} \right) \quad (17)$$

Due to the inclusion of the apparent inertia couple, θ will be nonzero at equilibrium. This causes these equations to lack a closed-form solution, although a solution can still be found using numerical methods. The chosen baseline values for the necessary constants are given in Table 1 and are based on the values for a subsonic circular parachute used by Eaton for experimentation. These values were selected to match with the values used by Eaton in his computer simulation.² This was done to facilitate comparison between the new dynamic modeling and the results provided in his paper, as described in Section IV. The baseline state solutions are given in Table 2.

Table 1. Baseline Parameters

Variable	Baseline Value
C_{T_α}	-0.1
C_{T_0}	0.7
$C_{N_\alpha} (\text{deg}^{-1})$	0.4
$D_P (m^2)$	6.5
$g (m/s^2)$	9.81
K_{11}	0.25
K_{33}	0.4
$m (kg)$	105.8
$z_{CG} (m)$	7.587
$\alpha_0 (deg)$	25
$\rho (kg/m^3)$	1.225

A sensitivity analysis was conducted to observe how the equilibrium conditions varied with the input. The apparent inertia coefficient, K_{33} , was varied while all other inputs were left at their baseline values. Figure 3 captures the variance in the equilibrium state with K_{33} . As K_{33} approaches 0.25, the baseline value of K_{11} , the apparent inertia couples drop out and the traditional solution from Eqs. (11), (12), and (13) is found. The angle of attack heavily relies on the value of K_{33} , whereas the velocity and theta do not vary substantially. Unlike the case without the apparent inertia couples, the parachute is not completely vertical while gliding. Outside of the range of K_{33} given, the only solution is the trivial non-gliding solution.

Table 2. Equilibrium State for Baseline Parameters

Variable	White-Wolf	Eaton
$u(m/s^2)$	3.610	0.534
$w(m/s^2)$	7.741	8.396
$V(m/s^2)$	8.541	8.413
$\alpha(deg)$	25	3.640
$\theta(deg)$	0	0.862

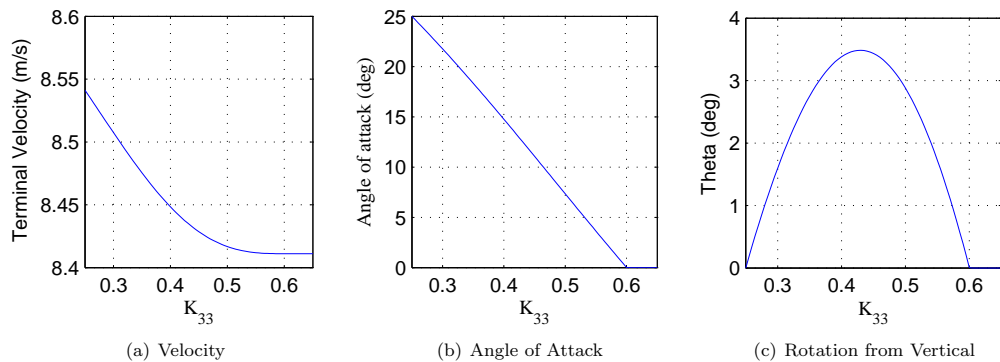
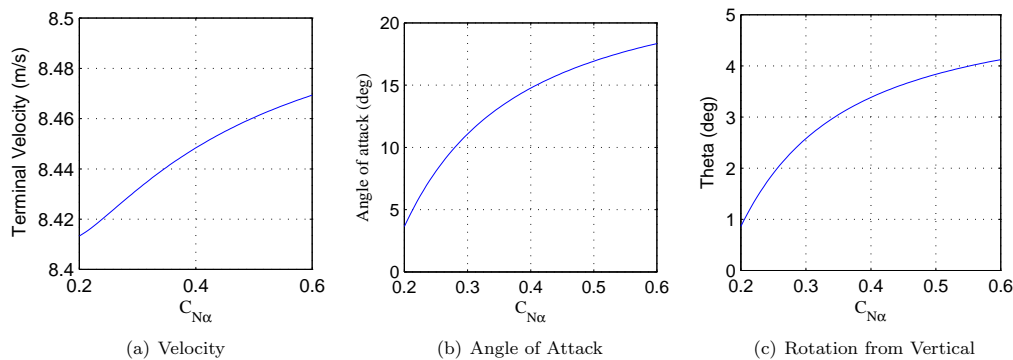
**Figure 3. Equilibrium state as a function of the apparent inertia constant K_{33} .**

Figure 4 displays the dependence of the equilibrium state on the normal force coefficient slope at the glide point, $C_{N\alpha}$. The angle of attack is observed to be a strong function of $C_{N\alpha}$, whereas the velocity and the Euler angle theta vary minimally. The effect of $C_{N\alpha}$ on equilibrium is of special importance to the stability argument as a minimum $C_{N\alpha}$ is often used to describe parachute stability.⁵ Unlike in the case without the apparent inertia couples where the equilibrium condition is fixed with respect to $C_{N\alpha}$, stability analyses must now include the change in the equilibrium state.

**Figure 4. Equilibrium state as a function of the normal force coefficient slope at the glide point.**

The effect of changing density was also inspected. Figure 5 shows that the density does have a significant effect on the terminal velocity, as expected. The angle of attack and θ , however, are constant as the density varies. This is difficult to see from inspecting Eqs. (14)–(17), however an analog to the equations without the apparent inertia terms can be made. In that case, changing density will cause a constant θ whereas both velocity components will be proportional to the inverse square root of the density, which will yield a constant angle of attack. If this is true for the equations with apparent inertia, then Eq. (16) will not depend on density as the implicit density terms within the $(A_{33} - A_{11})$ and uw terms will cancel. Therefore θ will be constant and the inverse square root dependence of u, w on density is true. This is significant to planetary

descent, as the orientation and angle of attack for the static stability point is not a function of the altitude even when the apparent inertia couples are included.

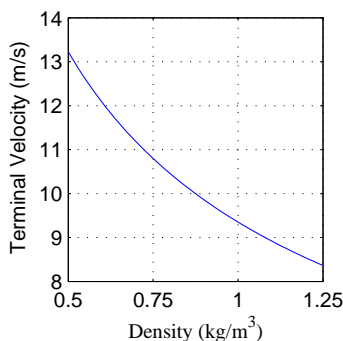


Figure 5. Equilibrium state as a function of the atmospheric density.

III. Small Disturbance Stability Analysis

A. Problem Formulation

The equations of motion were linearized around the equilibrium point. This was done by substituting small disturbance variables into the equations of motion, as shown in Eqs. (18)–(20). By neglecting higher order terms of the small disturbance variables and using the equilibrium equations given in Eqs. (14)–(17) to remove the equilibrium values, the linear equations of motion can be formed. These equations of motion are given by Eqs. (24)–(29) in the Appendix.

$$u = u_E + u' \quad (18)$$

$$v = v' \quad (19)$$

$$w = w_E + w' \quad (20)$$

⋮

By examining the linearized equations of motion, it becomes apparent that the longitudinal and lateral motions are decoupled. This allows the longitudinal motion governing u , w , q , and θ to be analyzed separately. The equations were transformed into matrix form as shown in Eqs. (21) and (22). The dynamic stability near the equilibrium state is then described by the eigenvalues of the matrix A_{long} .

$$\mathbf{x} = [u \ w \ q \ \theta]^T \quad (21)$$

$$\dot{\mathbf{x}} = A_{long} \mathbf{x} \quad (22)$$

Dynamic stability was tested by choosing a set of parameters and testing to see if any of the eigenvalues had positive real components. A computer script was written in MATLAB to find the boundary of stability by manipulating a chosen parameter to set the maximum real component of the eigenvalues to zero. The minimum C_{N_α} for stability was found as a function of the chosen parameters, as has been done in previous studies of parachute stability⁵ This minimum C_{N_α} was found as both a function of density and as a function of an apparent inertia scaling factor. This was done computationally as the variation on C_{N_α} affected both the local dynamics and the equilibrium point about which the equations are linearized.

B. Density Dependence Results

The results for the minimum allowable C_{N_α} for dynamic stability as a function of density are shown in Figure 6. It was found that the parachute becomes less stable as the atmospheric density increases. The changes in density directly affect the restoring forces and moments, which can cause increasing oscillations if too large. From the equilibrium study, it can be noted that variations in density do not affect the equilibrium point but they do have an effect on the stability of the equilibrium point. However, the equilibrium point

is still tied to the chosen C_{N_α} value. As expected, these results show that a parachute flight dynamics test must match the correct density to give accurate results about stability.

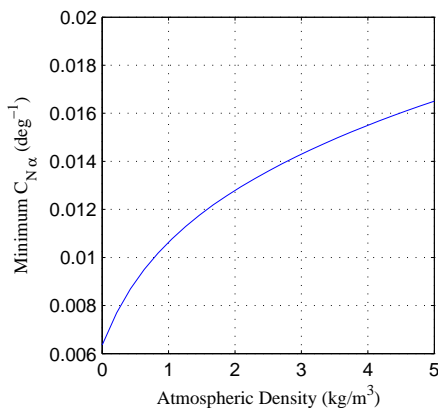


Figure 6. Minimum C_{N_α} for dynamic stability as a function of atmospheric density.

C. Apparent Inertia Dependence Results

The effect of apparent inertia on the the dynamic stability was a primary concern for these studies. The dynamic stability boundary was found as a function of an apparent inertia scale factor. This factor linearly scales all apparent inertia terms, as shown in Eq. (23). This can be seen as a way to model uncertainty in the apparent inertia terms, as it has been shown that they are difficult to measure accurately.^{2,3}

$$A_{i,j} = kA_{i,j,0} \quad (23)$$

Figure 7 shows the nearly linear dependence of the minimum C_{N_α} on the apparent inertia scale factor. It was found that the apparent inertia terms have a large effect on the dynamic stability. When neglecting apparent inertia ($k = 0$), it is found that the required C_{N_α} for stability is small but nonzero, which is similar to the White-Wolf dynamic stability analysis.⁵ It was found that the apparent inertia has a strong destabilizing effect, greatly increasing the requirements for dynamic stability. As the apparent inertia terms increase, the magnitude of the coupling moment increases. This moment acts in the direction that brings the system toward equilibrium, however as its magnitude increases, it can cause increasing oscillations around the equilibrium state leading to destabilization.

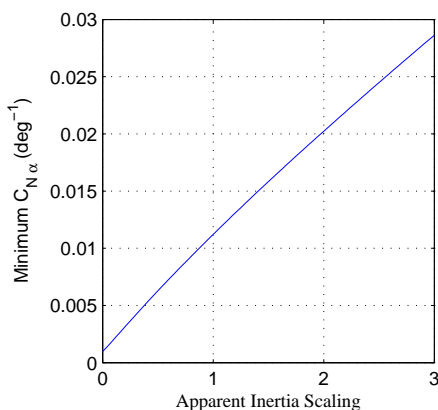


Figure 7. Minimum C_{N_α} for dynamic stability as a function of apparent inertia.

It may be suspected that the baseline ($k = 1$) apparent inertia values are too large, however it should be noted that all baseline parameters were determined experimentally.² Additionally, the baseline apparent inertia coefficients chosen are on the lower end of the range used by various dynamics models.³

IV. Computational Large Disturbance Stability Analysis

A. Simulator Creation

A six degree of freedom computational simulator has been developed to observe the motion of the system. This program was used to validate the linear stability predictions as well as to observe how these predictions perform for large disturbances.

The simulator was written to mimic the simulator discussed by Eaton² so that the program could be validated. The program was written in MATLAB using the built in Runge-Kutta variable step integrator. The simulators were compared using the baseline parameters and the initial conditions given in Tables 1 and 3. All other variables were taken to be zero so that the motion would be planar. An aerodynamics model using experimental data for a nonporous circular parachute¹⁰ was used. The comparison of the outputs is shown in Figures 13–15 in Appendix B. An aerodynamics model was also included for the payload. It was found that the simulated trajectories provided a good match to the outputs reported by Eaton. The small variances are likely due to the method used to implement the aerodynamics, as the Eaton model used a table lookup whereas the current simulator uses a polynomial approximation.

Table 3. Trajectory Comparison Initial Conditions

Variable	Initial Value
u (m/s)	-3
w (m/s)	5
θ (deg)	30

Once the simulator was verified against Eaton’s results, small modifications were made to adapt it to the posed stability problem. The canopy aerodynamics were set to the assumed aerodynamics model given by Eqs. (9) and (10) and both the payload aerodynamics and the empirical damping moment used by Eaton were neglected.

B. Results

For the computational stability results, the baseline constants from Table 1 were assumed as well as a constant density of 1 kg/m^3 . With these parameters, the minimum C_{N_α} for stability was found to be 0.012 deg^{-1} . Figure 8 displays the simulated motion when a small disturbance is given to the pitch angle for a stable system. As predicted, the disturbance is damped out and the system returns to the equilibrium state.

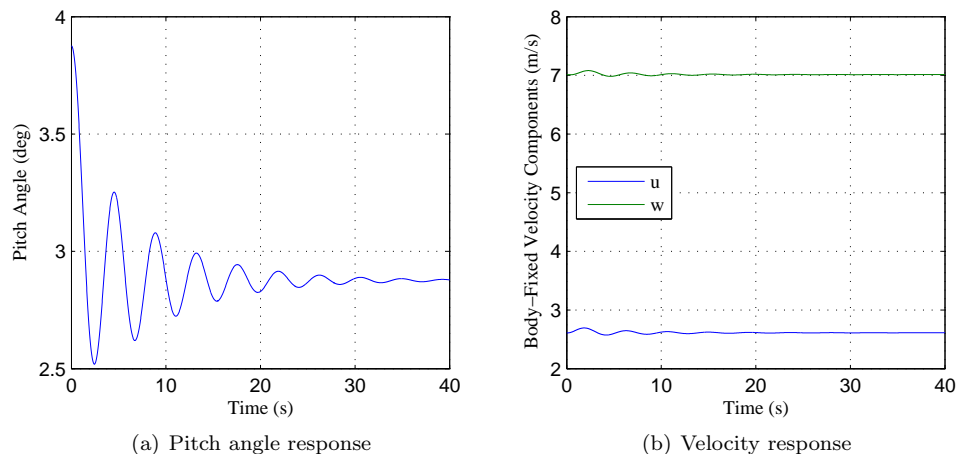


Figure 8. Response to a disturbance of $\theta' = 1^\circ$ with a stable $C_{N_\alpha} = 0.015 \text{ deg}^{-1}$.

Figure 9 shows that decreasing C_{N_α} below the predicted minimum causes the system to become unstable. Note that by decreasing C_{N_α} , the equilibrium point has been changed for this case. From these simulations, it can be seen that the stability predictions were accurate for this model.

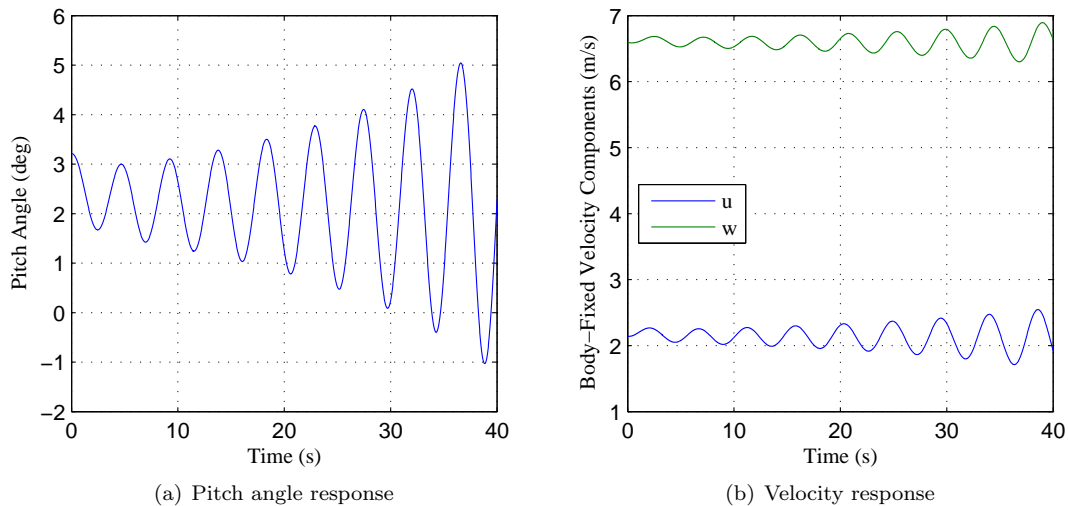


Figure 9. Response to a disturbance of $\theta' = 1^\circ$ with an unstable $C_{N_\alpha} = 0.010 \text{ deg}^{-1}$.

The behavior of the system was also analyzed for larger disturbances to observe how the small disturbance assumption affects the solution. Figure 10 shows the stable case with a disturbance of $\theta' = 10^\circ$. The pitching motion appears to be very similar for both the large and small disturbance cases, although the damping appears to be somewhat slower with the large disturbance. As expected, the velocity components are disturbed more with the large disturbance although they are still stable.

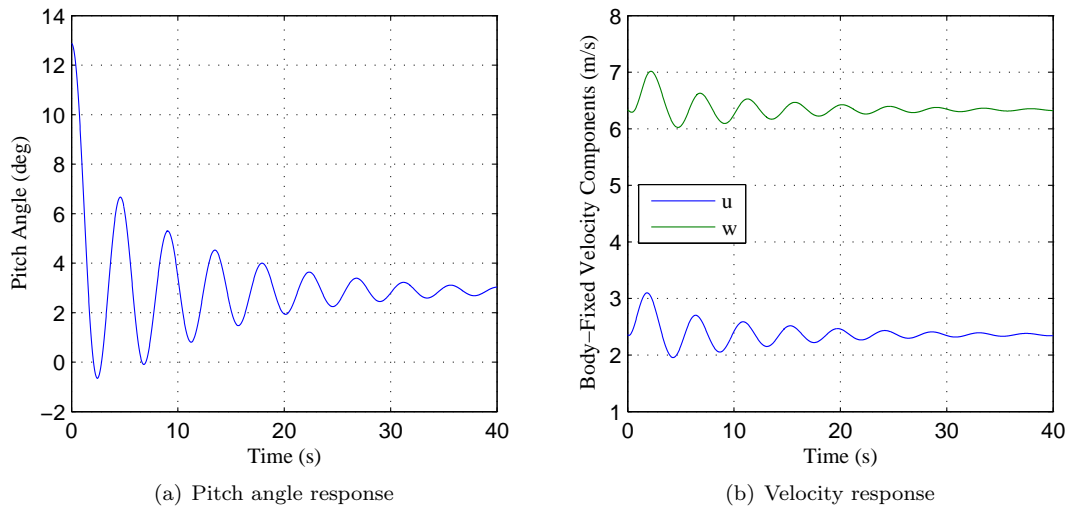


Figure 10. Response to a disturbance of $\theta' = 10^\circ$ with a stable $C_{N_\alpha} = 0.015 \text{ deg}^{-1}$.

The unstable system behavior with a large disturbance is given in Figure 11. Unlike in Figure 9, the instability is no longer characterized by an exponential increase away from the equilibrium position. The system oscillates a few times before it reaches a limit cycle where the parachute is descending while pitching back and forth. These pitching oscillations reach $\pm 35.7^\circ$, proving that the initial disturbance was considerably large.

Lateral stability was also computationally investigated. Figure 12 shows the system motion when a lateral disturbance is given. It was observed that with the baseline parameters, the system is laterally unstable. Despite using a C_{N_α} that predicts longitudinal stability, the lateral instability causes the system to enter a coning motion. The linear equations of motion predicted that the lateral and longitudinal motions would be

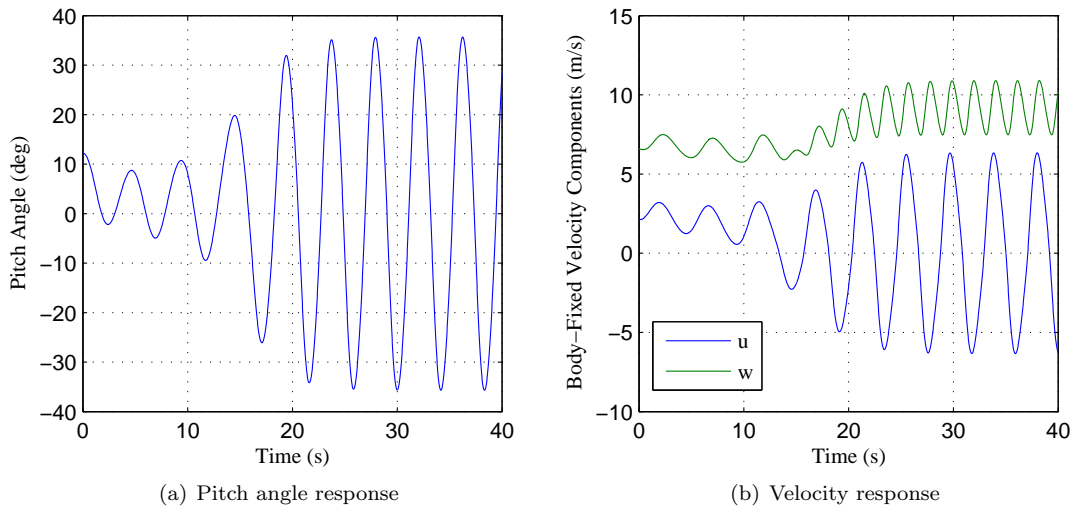


Figure 11. Response to a disturbance of $\theta' = 10^\circ$ with an unstable $C_{N_\alpha} = 0.010 \text{ deg}^{-1}$.

decoupled. This decoupling is observed for the first 5–10 seconds while the lateral variables are still small. It also appears that the total velocity increases, which is to be expected as the model is tracking the velocities at the canopy.

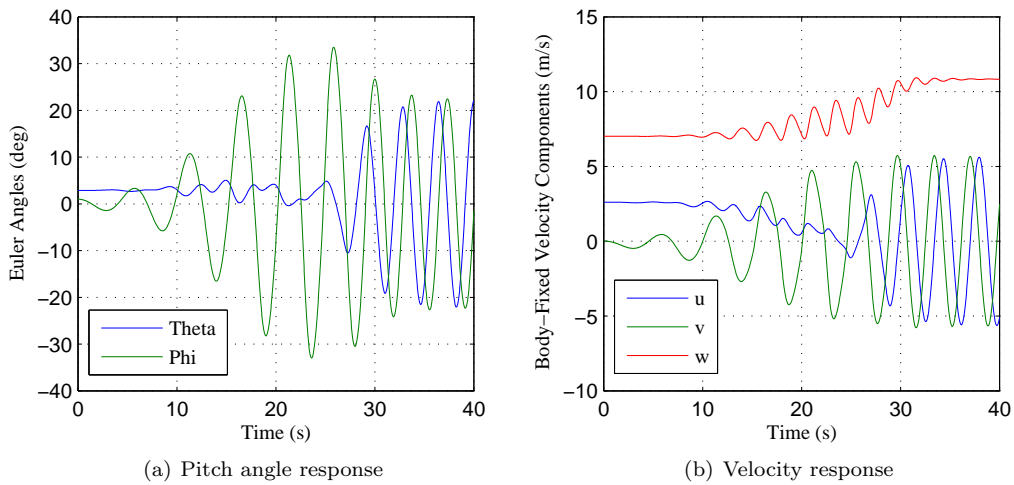


Figure 12. Response to a disturbance of $\phi' = 1^\circ$ with a longitudinally stable $C_{N_\alpha} = 0.015 \text{ deg}^{-1}$.

V. Conclusion

The static and dynamic stability of a parachute were analyzed for a set of equations of motion that include apparent inertia tensor effects. It was found that due to the addition of the apparent inertia terms, the equilibrium state was modified and that its solution was no longer closed form. The equilibrium state was calculated numerically and plotted as a function of multiple variables. The equations of motion were linearized about the equilibrium state and presented. The dynamic stability of the linear longitudinal motion was analyzed by finding the minimum slope of the normal force coefficient for stability. It was found that the system became more stable as density decreases and as the apparent inertia terms decrease. A simulator was created to integrate the nonlinear equations of motion. The small disturbance simulations agreed with the stability predictions made by the linear equations of motion. For large longitudinal disturbances, the stability predictions appeared to hold, although the unstable behavior became characterized by limit cycling. For the baseline case provided, it was found that the system was laterally unstable and that any lateral disturbances led to a coning motion.

Appendix A: Small Disturbance Equations of Motion

$$\begin{aligned} \dot{u}' = & \left[(m + A_{11}) - \frac{(K_1 + A_{15})^2}{I_{yy} + A_{55}} \right]^{-1} \left\{ - (m + A_{33})w_0q' \right. \\ & + \frac{K_1 + A_{15}}{I_{yy} + A_{55}} \left[(K_1 + A_{15})w_0q' - (A_{33} - A_{11})(w_0u' + u_0w') + mgz_{CG}\theta' \cos \theta_0 \right] \\ & \left. - mg\theta' \cos \theta_0 - \frac{1}{2}\rho A \left[C_{N_\alpha} \left(2\frac{\alpha_0}{\alpha_T} - 1 \right) (w_0u' - u_0w') + C_{N,T}(2u_0u' + 2w_0w') \right] \right\} \end{aligned} \quad (24)$$

$$\begin{aligned} \dot{v}' = & -u_0r' + (m + A_{11})^{-1} \left[(m + A_{33})w_0p' + mg\phi' \cos \theta_0 - \frac{1}{2}\rho A(u_0^2 + w_0^2)C_{N,T}\frac{v'}{u_0} \right] \\ & + \frac{K_1 + A_{15}}{m + A_{11}} \left[(I_{xx} + A_{55}) - \frac{(K_1 + A_{15})^2}{m + A_{11}} \right]^{-1} \left\{ (K_1 + A_{15}) \left[(m + A_{11})^{-1} \left[(m + A_{33})w_0p' \right. \right. \right. \\ & \left. \left. + mg\phi' \cos \theta_0 - \frac{1}{2}\rho A(u_0^2 + w_0^2)C_{N,T}\frac{v'}{u_0} \right] - w_0p' \right\} - (A_{33} - A_{11})w_0v' - mgz_{CG}\phi' \cos \theta_0 \end{aligned} \quad (25)$$

$$\begin{aligned} \dot{w}' = & (m + A_{33})^{-1} \left\{ (m + A_{11})u_0q' - mg\theta' \sin \theta_0 \right. \\ & \left. - \frac{1}{2}\rho A \left[(2u_0u' + 2w_0w') \left(C_{T_0} + \frac{1}{2}C_{T_\alpha} \alpha_T \left(\frac{\alpha_0^2}{\alpha_T^2} - 1 \right) \right) + C_{T_\alpha} \left(\frac{\alpha_0}{\alpha_T} \right) (w_0u' - u_0w') \right] \right\} \end{aligned} \quad (26)$$

$$\begin{aligned} \dot{p}' = & \left[(I_{xx} + A_{55}) - \frac{(K_1 + A_{15})^2}{m + A_{11}} \right]^{-1} \left\{ (K_1 + A_{15}) \left[(m + A_{11})^{-1} \left[(m + A_{33})w_0p' \right. \right. \right. \\ & \left. \left. + mg\phi' \cos \theta_0 - \frac{1}{2}\rho A(u_0^2 + w_0^2)C_{N,T}\frac{v'}{u_0} \right] - w_0p' \right\} - (A_{33} - A_{11})w_0v' - mgz_{CG}\phi' \cos \theta_0 \end{aligned} \quad (27)$$

$$\begin{aligned} \dot{q}' = & \frac{1}{I_{yy} + A_{55}} \left\{ - (K_1 + A_{15}) \left[\left((m + A_{11}) - \frac{(K_1 + A_{15})^2}{I_{yy} + A_{55}} \right)^{-1} \left[- (m + A_{33})w_0q' \right. \right. \right. \\ & + \frac{K_1 + A_{15}}{I_{yy} + A_{55}} \left[(K_1 + A_{15})w_0q' - (A_{33} - A_{11})(w_0u' + u_0w') + mgz_{CG}\theta' \cos \theta_0 \right] \\ & \left. - mg\theta' \cos \theta_0 - \frac{1}{2}\rho A \left[C_{N_\alpha} \left(2\frac{\alpha_0}{\alpha_T} - 1 \right) (w_0u' - u_0w') + C_{N,T}(2u_0u' + 2w_0w') \right] \right] + w_0q' \right\} \\ & + (A_{33} - A_{11})(w_0u' + u_0w') - mgz_{CG}\theta' \cos \theta_0 \end{aligned} \quad (28)$$

$$\dot{r}' = 0 \quad (29)$$

Appendix B: Simulator Output Comparison Plots

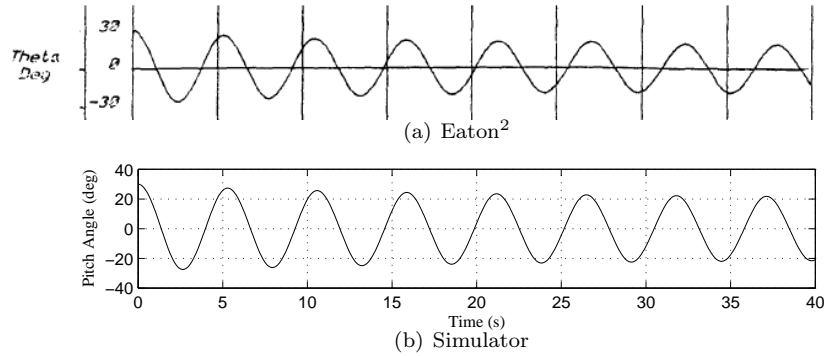


Figure 13. Comparison of pitch angle responses for baseline trajectory.

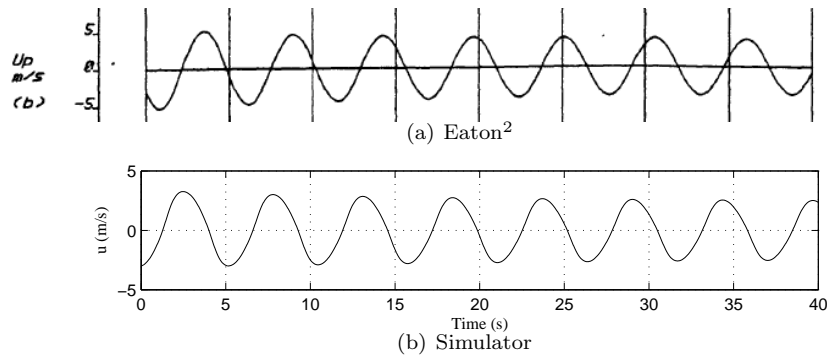


Figure 14. Comparison of velocity component in the x direction responses for baseline trajectory.

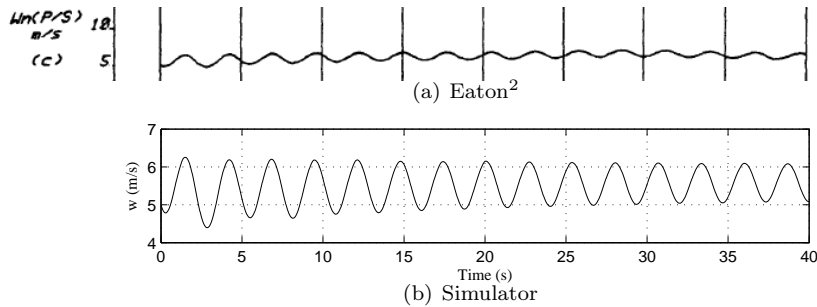


Figure 15. Comparison of velocity component in the z direction responses for baseline trajectory.

Acknowledgments

Part of this research was carried out at the Jet Propulsion Laboratory, California Institute of Technology, under a contract with the National Aeronautics and Space Administration.

References

- ¹Gallon et al., "Low Density Supersonic Decelerator Parachute Decelerator System," 22nd AIAA Aerodynamic Decelerator Systems Technology Conference, Daytona Beach, FL, 2013.
- ²Eaton, J.A., "Validation of a Computer Model of a Parachute," Ph. D. Dissertation, University of Leicester, Leicester, UK, 1982.
- ³Dobrokhodov, V.N., Yakimenko, O.A., and Junge, C.J., "Six-Degree-of-Freedom Model of a Controlled Circular Parachute," *Journal of Aircraft*, Vol. 40, No. 3, 2003, pp. 482–493.
- ⁴Tory, C., and Ayres, R., "Computer Model of a Fully Deployed Parachute," *Journal of Aircraft*, Vol. 14, No. 7, 1977, pp. 675–679.
- ⁵White, F.M., and Wolf, D.F., "A Theory of Three-Dimensional Parachute Dynamic Stability," *Journal of Aircraft*, Vol. 5, No. 1, 1968, pp. 86–92.
- ⁶Cruz et al., "Parachute Models Used in the Mars Science Laboratory Entry, Descent, and Landing Simulation," 22nd AIAA Aerodynamic Decelerator Systems Technology Conference, Daytona Beach, FL, 2013.
- ⁷Featherstone, R., *Rigid Body Dynamics Algorithms*, Springer, New York, 2008, pp. 32–35.
- ⁸Ibrahim, S., "Experimental Determination of the Apparent Moment of Inertia of Parachutes," University of Minnesota, Minneapolis, MN, 1964.
- ⁹Yu, Y. , "Virtual Masses and Moments of Inertia of Disks and Cylinders in Various Liquids," *Journal of Applied Physics*, Vol. 13, 1942, pp. 66–69
- ¹⁰Ayres, R.M., "The Simulation of the Descent Characteristics of Fully Inflated Subsonic Parachutes," University of Leicester Engineering Department Report, July 1974.